

# Modelling non-volcanic tremor, slow slip events and large earthquakes in the Guerrero subduction zone (Mexico) with space-variable frictional weakening and creep

Dimitri Zigone,<sup>1</sup> Yehuda Ben-Zion<sup>1</sup> and Michel Campillo<sup>2</sup>

<sup>1</sup>*Department of Earth Sciences, University of Southern California, Los Angeles, CA 90089-0740, USA. E-mail: zigone@usc.edu*

<sup>2</sup>*Institut des Sciences de la Terre, Université Joseph Fourier; CNRS, IRD, BP 53, F-38041 Grenoble, France*

Accepted 2015 April 16. Received 2015 April 15; in original form 2014 November 25

## SUMMARY

We explore with numerical simulations basic physical conditions leading to key observed features of non-volcanic tremor (NVT) in relation to slow slip events (SSEs) and earthquakes along the Guerrero segment of the Mexican subduction zone. To study the interactions between different modes of slip, and examine possible variations over timescales larger than the 15 year observational interval, we use a model with a planar interface governed by space-varying static/kinetic friction and dislocation creep in a 3-D elastic solid. A fault section with zero weakening during frictional slip fails in a mode corresponding to a ‘critical depinning transition’ that produces generically many observed features of NVT. A patch with elevated creep coefficients represents a section with SSE. Simulations with small added stress oscillations are used to examine triggering of NVT by large remote earthquakes. The results reproduce well the basic observed properties of NVT and SSE in the Guerrero area, while pointing to complex interactions between large earthquake cycles, quasi-period SSE and scale-invariant NVT behaviour. The model simulations provide additional information on expected frequency-magnitude statistics, slip distributions and space–time properties of the different event types that may be tested with accumulation of future data. Some earthquake and NVT events near the opposite sides of the SSE patch have significant separation between their hypocentres and centroids. The rates of these events are correlated with the creep evolution in the SSE section. The results also suggest that aseismic deformation in the area may have transients on timescales larger than the observational period.

**Key words:** Phase transitions; Earthquake dynamics; Earthquake interaction, forecasting, and prediction; Statistical seismology; Rheology and friction of fault zones.

## 1 INTRODUCTION

Slow slip events (SSEs) and non-volcanic tremor (NVT) are transient phenomena that have been observed within the brittle-ductile transition regime of various subduction zone interfaces (e.g. Peng & Gomberg 2010; Rubinstein *et al.* 2010; Beroza & Ide 2011). The SSE are characterized by aseismic slip on the fault interface and are sometimes accompanied by NVT episodes consisting of weak, long-duration, seismic signals that are coherent over many stations (Obara 2002). The correlation between these two phenomena was established clearly with the so-called Episodic Tremor and Slip (ETS) in Cascadia (Rogers & Dragert 2003) and southwest Japan (Obara *et al.* 2004). Correlated ETS appear to exist in other subduction zones including Alaska (Ohta *et al.* 2006; Peterson & Christensen 2009), Costa Rica (Brown *et al.* 2005; Outerbridge *et al.* 2010) and Mexico (e.g. Payero *et al.* 2008; Kostoglodov *et al.* 2010). However, NVT events can also occur without SSE in a form

of ongoing/background activity (e.g. Wech *et al.* 2009; Obara *et al.* 2011; Husker *et al.* 2012). An interesting aspect of NVT, which indicates proximity to a critical state, is their sensitivity to triggering by various small loadings such as tides (e.g. Rubinstein *et al.* 2008; Thomas *et al.* 2009) and remote earthquakes (e.g. Ghosh *et al.* 2009; Peng *et al.* 2009; Zigone *et al.* 2012).

The discovery of SSE and NVT is relatively recent so only 10–15 yr of data are available. This prevents examining with in-situ data some key issues, such as the stability of various observed features over longer time scales. This limitation can be partially overcome using laboratory experiments (e.g. Voisin *et al.* 2008; Burlini *et al.* 2009; Zigone *et al.* 2011) and numerical modelling (e.g. Liu & Rice 2009; Yamashita 2013). Most efforts to model SSE and NVT have been based on rate-state friction and fluids effects, using constitutive laws with 5–10 parameters (or more) that have to be carefully tuned to explain a subset of the observed phenomenology (e.g. Segall *et al.* 2010; Rubin 2011). While these models provide insights into aspects

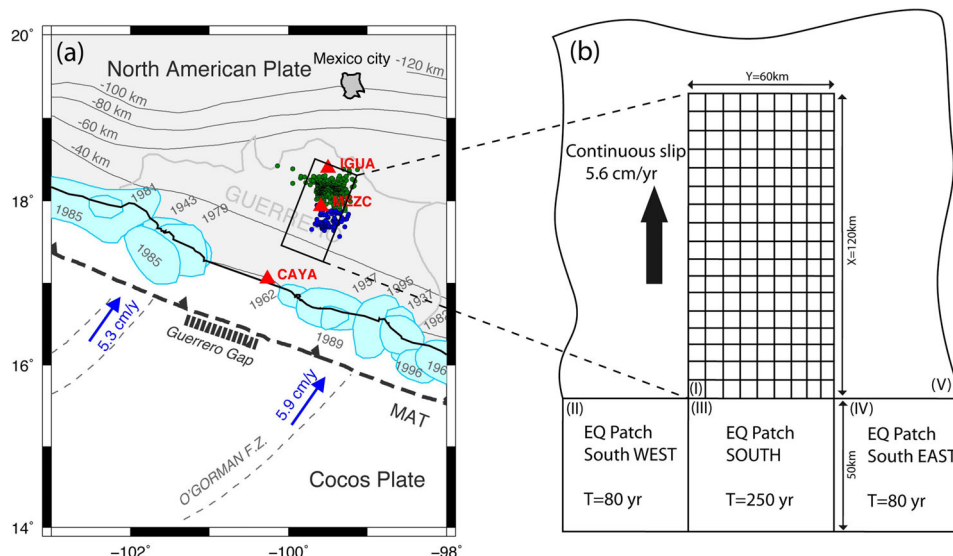


**Figure 1.** (a) Seismotectonic map of Guerrero, Mexico. The blue arrows indicate the direction and velocity in cm/yr of the NUVEL relative plate motion between the Cocos and North American Plate (DeMets *et al.* 1994). Blue patches represent major earthquake rupture zones. Thin grey lines show isodepth contours of the subducted oceanic slab (after Pardo & Suarez 1995). Dots show the NVT locations obtained by Husker *et al.* (2012) in two different regions: blue dots in the region close to the section of the interface affected by SSE and Green dots for the NVT located further down dip the subduction in the so-called NVT sweet spot (Husker *et al.* 2012). The red triangles are the GPS stations. The black rectangle indicates the modelled portion of the subduction zone. (b) Computational grid and boundary conditions for the Guerrero area. The computation grid (region I) is 120 km long and 60 km wide. It is bounded by three large earthquake patches on the southern side (regions II, III and IV) and creeping regions with plate velocity of  $5.6 \text{ cm yr}^{-1}$  elsewhere (region V). The entire fault interface is surrounded by a 3D elastic solid. Regions II and IV represent subduction earthquakes with a recurrent time of 80 yr, while Region III represents the Guerrero seismic gap with a recurrent time of 250 yr. For easier visualization, the computational grid is rotated by  $90^\circ$  clockwise in subsequent figures.

of the involved processes, it is desirable to have a basic explanation ('simple model with minimal parameters') for the essential physics that distinguishes NVT and ETS from regular earthquakes.

Building on previous analytical and numerical works, Ben-Zion (2012) showed that reducing the difference between static and dynamic friction levels toward zero is sufficient to produce a transition of multiple phenomena and scaling relations from those characterizing regular earthquakes to those associated with NVT. The difference between static and dynamic strength levels, quantified by a non-dimensional strength-change parameter  $\varepsilon_D$  defined in the next section, is a tuning parameter of the mode of failure and related response functions of an interface subject to slow remote loading (Fisher *et al.* 1997; Dahmen *et al.* 2009; Ben-Zion *et al.* 2011). A fault section characterized by  $\varepsilon_D < \varepsilon_c \sim 0$  fails by an ongoing sequence of 'slip avalanches' associated with a second order (critical) transition in the state of the interface referred to as *critical depinning transition* (Fisher *et al.* 1997; Ben-Zion 2012). The failure events associated with the critical depinning transition are predicted to have scale-invariant properties in space, time and size (other than 'finite-size' corrections discussed further below). In contrast, a fault section having  $\varepsilon_D > \varepsilon_c$  (i.e. standard slip or strain weakening) fails by a sequence of unstable events having properties of regular earthquakes (e.g. Ben-Zion & Rice 1993; Ben-Zion 1996; Ben-Zion *et al.* 2003).

Fisher *et al.* (1997) showed with renormalization group theory that the large-scale behaviour of a fault under slow remote loading (spatio-temporal slip and seismicity patterns, scaling relations, frequency-size statistics, etc.) depends only on the value of  $\varepsilon_D$ , and not on details of the transition from static to dynamic failure levels, at least for the class of rheologies associated with monotonic functions (see also Dahmen & Ben-Zion 2009, and references therein). The simplest way to analyze the large-scale behaviour of a fault

having different values of  $\varepsilon_D$  is to use static/kinetic friction. As discussed by Ben-Zion & Rice (1993, 1995) and others, this renders the fault inherently-discrete, which provides an effective means for modelling a fault with strong heterogeneities that prevent large-scale rupture processes from being smooth and continuous (see section 5 of Ben-Zion (2008) for additional details).

In the present paper we use a model similar to that of Ben-Zion (2012), with a planar interface governed by space-varying static/kinetic friction and dislocation creep, to explore the range of conditions leading to key observed features of NVT in relation to SSE and regular earthquakes along the Guerrero segment of the Mexican subduction zone (Fig. 1a). The employed model realization is tailored with choices of dimensions, rheological properties and boundary conditions to the Guerrero segment, using the existing knowledge on the geometry and recent behaviour of the study region. Although it has been claimed that fluid migration plays a role in the dynamic evolution of the interface, we investigate here a model involving only time-independent fault properties and long range elastic interactions. Our goal is to provide a simple framework that can explain and predict multiple general features related to NVT, SSE and earthquakes in the context of the Guerrero region, rather than to reproduce or fit a subset of specific observations.

The Guerrero segment produced some of the largest SSE recorded so far, with four events during the last 16 yr (1998, 2002, 2006 and 2009–2010) involving southward surface displacement up to 5–6 cm per SSE and equivalent magnitude up to 7.6 Mw (Kostoglodov *et al.* 2003; Cotte *et al.* 2009; Vergnolle *et al.* 2010; Radiguet *et al.* 2011, 2012). These SSE, with apparent durations of about 6 months, have been accompanied by strong activity of NVT in central Guerrero (Payero *et al.* 2008) where the subduction interface remains horizontal (Fig. 1a) at 41 km depth for distances between 150 and 250 km from the coast (e.g. Pardo & Suarez 1995;

Perez-Campos *et al.* 2008). The NVT are located at two different regions, one close to the section of the interface affected by SSE (blue dots in Fig. 1a) and the second further down dip referred by Husker *et al.* (2012) as the NVT sweet spot for its almost continuous activity (green dots on Fig. 1a).

Frank *et al.* (2013) detected low-frequency earthquakes (LFEs), which are small amplitude short duration impulsive seismic events that correspond at least partially to NVT (Shelly *et al.* 2007), within the tremor period of activity. They located them on the subduction interface with a low-dipping focal mechanism consistent with the geometry and the convergence in Guerrero. Zigone *et al.* (2012) and Rivet *et al.* (2014) observed during the 2009–2010 SSE a temporal correlation between NVT activities, SSE slip rates and seismic velocity changes, suggesting possible complex interactions between these phenomena. Zigone *et al.* (2012) also discussed NVT in Guerrero that were triggered by the 8.8 Mw Maule earthquake. The subhorizontal geometry in Guerrero allows the use of a simple flat frictional interface (black rectangle in Fig. 1a) to model the dynamics of NVT, SSE and earthquakes in that region. In the next section we outline the rheology, geometry, stress interactions and boundary conditions used to model the Guerrero segment of the Mexican subduction zone. We then present basic features of simulated NVT, SSE, earthquakes and events triggered by passing waves. The results duplicate the key observed phenomena and show additional features including different events statistics in different fault sections and long-term temporal changes in the behaviour of the simulated SSE.

## 2 MODEL

We use a model similar to that of Ben-Zion (2012), with a cellular planar interface governed by static/kinetic friction and dislocation creep in a 3D surrounding elastic solid. The fault includes a computational grid (region I of Fig. 1b) where evolving fields are generated in response to ongoing loading imposed as slip boundary conditions on the other fault regions (regions II–V of Fig. 1b). The model configuration of Ben-Zion (2012) corresponds to a vertical strike-slip fault. To adapt the model for the present purpose, we locate the (top part of the) computational grid 350 km below the free surface and transform variables so that the original strike-slip motion represents horizontal motion along the  $x$ -coordinate in Fig. 1(b). By using appropriate boundary conditions around the computational grid we simulate the convergence between the Cocos and North American Plates at the Guerrero subduction zone region.

The stress on the computational grid, generated by the boundary conditions and failing grid cells, is computed with a discretized boundary integral equation:

$$\tau(i, j, t) = \sum_{k,l} K(i, j, k, l) [V_{pl}t - u(k, l, t)], \quad (1)$$

where the matrix  $K(i, j, k, l)$  gives the stress at cell  $(i, j)$  due to a uniform unit right-lateral slip at cell  $(k, l)$ , and the ‘source term’ in the square bracket is the slip deficit of cell  $(k, l)$  at time  $t$  with respect to the plate motion. In numerical simulations the employed  $K(i, j, k, l)$  is based on the solution for dislocations in a 3D elastic half-space (Ben-Zion & Rice 1993). The total slip at each cell is the sum of two contributions: slow creep between earthquakes and rapid brittle motion during the occurrence of earthquakes (Ben-Zion 1996). The creep process is controlled by a power-law dependence of creep velocity on the local stress:

$$V_c(x, y, t) = c(x, y) \cdot \tau(x, y, t)^3, \quad (2)$$

where  $c(x, y)$  is a distribution of space-dependent coefficients that control the amplitude of the creep for a given stress level. The brittle failure process is controlled by spatial distributions of static friction  $\tau_s$ , dynamic friction  $\tau_d$  and arrest stress  $\tau_a$  related as follows. When the stress at any position reaches the static friction, the strength changes to  $\tau_d$  for the remaining duration of the event and the stress drops locally to the arrest level  $\tau_a$ , which may be lower than  $\tau_d$  to accommodate dynamic overshoot (Ben-Zion & Rice 1993). The values of  $\tau_s$ ,  $\tau_d$  and  $\tau_a$  are connected by the strength-change parameter  $\varepsilon_D$ :

$$\varepsilon_D = \frac{\tau_s - \tau_d}{\tau_s - \tau_a}. \quad (3)$$

As mentioned in Section 1,  $\varepsilon_D$  is a key model parameter that can be tuned to produce earthquake-type failures and tremor-like slip instabilities on the fault. On an infinite interface under slow remote loading, the limit neutral value  $\varepsilon_D = 0$  leads to a failure mode associated with a critical depinning transition of the interface (Fisher *et al.* 1997; Dahmen *et al.* 2009). Situations with  $\varepsilon_D > 0$  represent dynamic weakening leading to brittle instabilities, while cases with  $\varepsilon_D < 0$  represent dynamic strengthening leading to stable slip (Mehta *et al.* 2006; Ben-Zion *et al.* 2011). A finite interface under slow ongoing loading fails via critical depinning if  $\varepsilon_D < \varepsilon_c \sim 0$ ; the value of  $\varepsilon_c$  depends on system-specific details and may be estimated numerically for the system at hand (e.g. fig. 5 of Ben-Zion 2012). The critical value  $\varepsilon_D < \varepsilon_c$  may be understood as the spatial average of small positive and negative  $\varepsilon_D$  on a fault section having a mixture of patches with slight weakening and strengthening rheologies; this regime may also represent a section where the healing of strength recovery to  $\tau_s$  is faster than the stress transfer from other failing regions (Ben-Zion 2012).

During slip at any location, due to unstable motion or creep, the stress is redistributed everywhere according to eq. (1). If the stress transfer during a model event increases the stress at other cells to their static or dynamic strength thresholds, as appropriate, these cells fail generating additional local slip. When the stresses at all cells are below the brittle failure thresholds, the event ends and the brittle strength at all failing cells recovers back to  $\tau_s$ . The scalar seismic potency (integral of slip over the failure area) and other quantities of the simulated brittle events are computed from the seismic slip distribution on the fault. The magnitudes are calculated from the potencies using the empirical quadratic potency-magnitude scaling relation of Ben-Zion & Zhu (2002). The creep-slip accumulates gradually in the time intervals between model earthquakes at different fault positions based on eq. (2). Significant episodes of creep-slip that propagate along the fault on time scales of days to weeks are considered to represent SSE.

The model dimensions, boundary conditions, and values of  $\varepsilon_D$  and the creep coefficients  $c(x, y)$  are chosen to represent the situation of the Mexican subduction zone (Figs 1b and 2). A 60 km  $\times$  120 km horizontal computational grid, embedded in a 3D elastic solid, is discretized into 28 800 square cells, each with an area of 550 m<sup>2</sup> (region I in Fig. 1b). This represents the near-horizontal portion of the subduction interface in Guerrero at a depth of 41 km (e.g. Pardo & Suarez 1995; Perez-Campos *et al.* 2008). It is surrounded on the sides and to the NE by portions of an interface (region V in Fig. 1b) that creep at constant velocity of 5.6 cm yr<sup>-1</sup>, which corresponds to the convergence rate between the Cocos plate and the North American plate in this region (DeMets *et al.* 1994). The computational grid is bounded on the SW side by three locked patches (regions II, III, IV in Fig. 1b) with imposed staircase slip histories that represent ruptures zones of large subduction earthquakes along

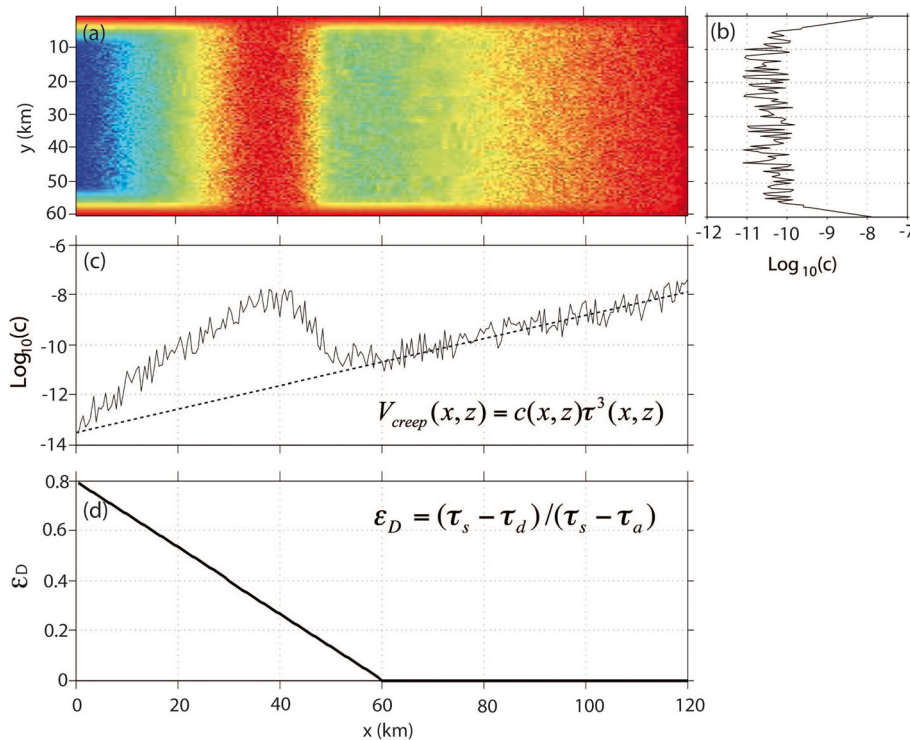


**Figure 2.** Assumed friction and creep parameters. (a) Distribution of the creep parameter  $c(x, y)$  on the computational grid with red and blue representing high and low values, respectively. Note the presence of a high creeping section between  $25 < x < 45$  km that represents the section of the interface sustaining SSE. (b) Cross section of  $c(x, y)$  along  $x = 60$  km. (c) Cross section of  $c(x, y)$  along  $y = 30$  km. (d) Distribution of the strength-change parameter  $\epsilon_D$  along the  $x$ -axis. The sections with positive and near-zero  $\epsilon_D$  represent the seismogenic and critical portions of the fault, respectively.

the Mexican trench. In regions II and IV, the recurrence time between each imposed earthquake is 80 yr. In region III that represents the Guerrero seismic gap, we assume a recurrence time of 250 yr (e.g. Singh *et al.* 1981; Nishenko & Singh 1987; Anderson *et al.* 1989).

We use the same basic functional forms for the space-variations of the frictional strength and creep coefficients as in Ben-Zion (2012), modified as follows to represent the study area. The static friction is given by  $\tau_s = C + f_s \sigma_n$ , with  $f_s = 0.75$ , cohesion  $C = 10$  Mpa and  $\sigma_n = 738$  MPa for an horizontal interface at 41 km depth. The local arrest stress is given from the static friction with uncorrelated random fluctuations as  $\tau_a = \tau_s - 3 \text{ MPa} \pm 1 \text{ MPa}$ . For easier visualization of results, the grid is rotated by  $90^\circ$  clockwise in the remaining figures with  $x$  and  $y$  corresponding to the along-dip and along-strike directions, respectively. The Mexican trench is on the left on all subsequent figures with results on the fault.

To fix the values of the strength-change parameter  $\epsilon_D$  and creep coefficients  $c(x, y)$  (see Fig. 2) we utilize constraints from observational results. Radiguet *et al.* (2012) used inversion of Global Position System (GPS) measurements and found a strong seismic coupling ( $>0.7$ ) in the seismogenic zone and a decreasing coupling in the subhorizontal portion of the plate to values around 0.2 at 180 km from the coast. The values of  $c(x, y)$  are prescribed to increase overall as a power law along the fault from SW to NE perpendicular to the trench (dashed line in Fig. 2c). This is modified to represent the section of the Guerrero subduction interface where SSE are recorded (Radiguet *et al.* 2012, and references therein) by using higher creeping coefficients on the first 50 km of the computational grid (solid black line in Fig. 2c). We also add 3 per cent random variations to  $c(x, y)$  to represent heterogeneities at the interface. The heterogeneities produce small-scale stress concentrations

that increase the number of brittle failure events. Higher/lower values of these random variations lead to more/less events per model year, but the precise value does not affect the main aspects of the results. Finally, to reduce edge effects between the computational grid and other portions of the interface,  $c(x, y)$  increases exponentially at the edges of the computational grid (Fig. 2b). To model a transition from earthquake-type failures to NVT, we assume that  $\epsilon_D$  decreases linearly from 0.8 at the left edge of the computational grid to 0 at  $x = 60$  km and stays zero for higher  $x$  positions (Fig. 2d).

The model is implemented in FORTRAN 77 and the computational effort is proportional to  $N^2$ , with  $N$  being the number of grid cells, average time step between brittle instabilities (related to the assumed cell size and frictional properties), average time step for creep calculations between brittle events, and total duration of the simulated data. The time steps between brittle instabilities are variable and are chosen so that each event begins with a single hypocentre (Ben-Zion & Rice 1993). The time steps for creep calculations are the intervals between brittle events or 3 days if smaller (Ben-Zion 1996), but are reduced to 0.1 sec for the triggering sequences describes in Section 3.5. The resulting computational cost is about 1.6 hr on a single CPU per typical year of model evolution, while each of the triggering sequences requires about 10–12 hr to compute 15 min of model evolution. For the grid used in this study (28 800 computational cells), the runtime memory requirement is about 500 Mb.

### 3 RESULTS

Using the model described in the previous section, we simulate unstable events (earthquakes and NVT) and propagating creep on the computational grid. The unstable events have local magnitudes

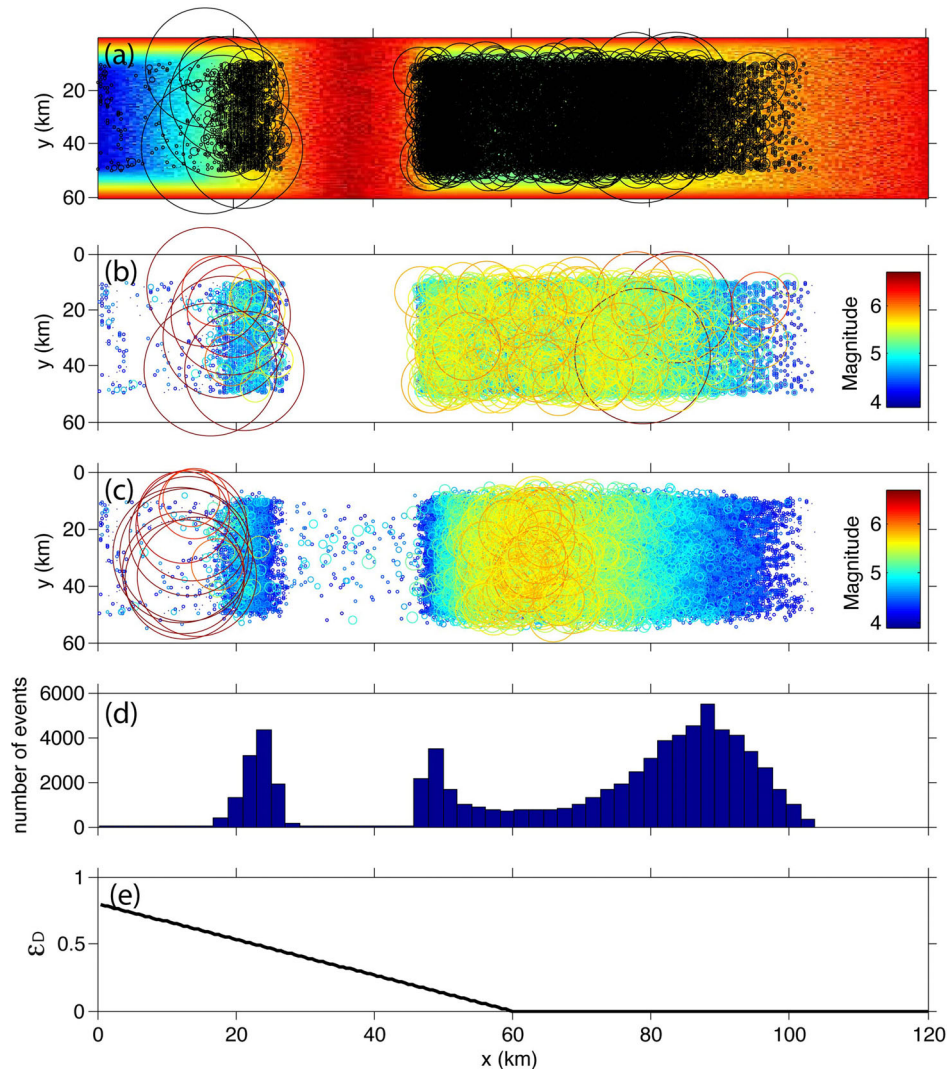


**Figure 3.** (a) Hypocentre locations of model instability events with circle size proportional to the failure area of each event. The background colours indicate the distribution of the  $c(x, y)$  on the fault. (b) Same as (a) with colours indicating the magnitude of each event. Note the lack of hypocentres in the SSE patch. (c) Centroids of the instability events on the fault with colours indicating magnitudes. (d) Histogram of the number of events along the  $x$ -axis. Note the bimodal distribution of the events after the gap corresponding to the SSE patch ( $x > 46$  km). (e) Distribution of  $\varepsilon_D$  along the  $x$ -axis.

$M$  in the range 3.8–6.7. The minimum and maximum magnitudes are determined, respectively, by the sizes of the numerical cell and overall computational grid, and to some extent also by the event stress drops (e.g. Ben-Zion & Rice 1993, 1995). Refining the cell size and increasing the size of the computational grid will increase the magnitude range, but at the expense of higher computational effort. The early period of simulated history is associated with transient behaviour that is dominated by the initial conditions. To focus on a time interval where the stress on the fault is self-organized in relation to the assumed properties, we ignore the first 135 yr of model simulations and analyze results from the subsequent 90 yr. The large earthquake patches to the SW and SE of the computation grid (regions II and IV in Fig. 1b) break 23 yr into the examined simulation period.

### 3.1 Spatial event distribution

Figs 3(a) and (b) display the spatial distribution of 71 566 hypocentres (coloured dots and circles) of slip instability events (earthquakes and tremors) on the computational grid during 90 yr of model evolu-

tion. Fig. 3(a) shows the hypocentres on the background of the used  $c(x, y)$  parameters (Fig. 2a) and Fig. 3(b) indicates the event magnitudes. The size of the circles is proportional to the rupture area of the events. Fig. 3c provides additional information by presenting the centroid locations of the slip distributions of the instability events, which give better indicators on the slip extent of each event. Figs 3(d) and (e) present, respectively, the number of simulated events and assumed  $\varepsilon_D$  value along the  $x$ -coordinate.

The spatial distribution of the hypocentres is not uniform along the fault but varies in relation to  $\varepsilon_D$  and  $c(x, y)$ . A notable feature in Figs 3(a) and (b) is a gap without any hypocentres in the central part of the fault from  $x = 30$  km to  $x = 46$  km. As shown on Fig. 3(a), this gap is correlated with the high values of  $c(x, y)$  used to model an SSE patch along the interface (Section 2). Because of these large values of  $c(x, y)$ , all the deformation in this region is relaxed through slow aseismic creep. While this is expected, the interaction with the other events on the fault leads to episodic behaviour of higher slip velocity that are reminiscent of the SSEs recorded in Mexico. The characteristics and properties of the creep slip in relation to the GPS data in the area are discussed in more detail in Section 3.3.

The gap of seismicity associated with the SSE patch is bounded by two active regions that concentrate all the hypocentres (Fig. 3b). The characteristics of these regions vary along the  $x$ -axis as  $\varepsilon_D$  decreases. The first region is located on the southern section of the fault, from  $x = 0$  to  $x = 30$  km, where  $\varepsilon_D > 0$ . It includes most of the largest magnitude earthquakes with eight of the eleven  $M > 6$  events (large red circles in Fig. 3b). The remaining three  $M > 6$  events with hypocentres around  $x = 80$  km are discussed below. The large magnitude events are surrounded by thousands of smaller instability events in the background (small blue circles and dots in Fig. 3b). Most of this microseismicity occurs around  $x = 20$ – $25$  km at the edge of the SSE area with additional scattered events from  $x = 0$  to  $x = 20$  km. As discussed further in Section 3.2, all of these events show classical properties and scaling relations of regular earthquakes, rendering this section of the fault a typical seismogenic zone (Ben-Zion 2008, 2012).

The second region of seismicity is located at the northern section of the fault beyond the SSE patch ( $x > 46$  km) where  $\varepsilon_D \approx 0$ . It has tens of thousands of distributed hypocentres with lower magnitudes compared to the seismogenic section on the other side of the SSE patch (Fig. 3b). The hypocentre density and event magnitudes are relatively uniform up to around  $x = 90$ – $100$  km, where both decrease because of the increasing  $c(x, y)$  in that region. The (near-) zero  $\varepsilon_D$  in this section produces unstable events that are part of a critical depinning transition of the interface (Ben-Zion 2012). The properties of these events are discussed in Section 3.2. In the following we refer to this section as the critical portion of the fault.

The spatial distribution of the centroids of the instability events (Fig. 3c) has the same two regions of activity discussed above, but the SSE patch with seismicity gap has a few centroids. The use of the centroid locations reveals additional details on the behaviour of the modelled subduction zone. In particular, the centroids of all  $M > 6$  instability events are concentrated around  $x = 15$  km in the seismogenic portion of the fault (large red circles in Fig. 3c), including the three events that initiated in the critical region with  $\varepsilon_D = 0$  and have hypocentre locations around  $x = 80$  km (Fig. 3b). This confirms that the slip of all major brittle failure events is concentrated in the southern seismogenic section ( $x < 25$  km) of the fault where  $\varepsilon_D > 0$ . The discrepancy between the hypocentre and centroid locations is explained by the complexity of the slip distributions of the instability events in the critical fault section. For these three  $M > 6$  events, the initial failure generates fractal slip patches in the critical section, which lead (in these cases) to continuing failure in the seismogenic section with larger crack-like slip distributions. This is discussed further and illustrated in the next section. Similar situations explain why a few centroids are located in the SSE patch (Fig. 3c). In these cases, the events are composed of discontinuous clusters of slip patches, one located in the seismogenic zone and the other in the critical section. The resulting centroids are located somewhere in between, that is, in the SSE patch.

Fig. 3(c) also show more spatial clustering of instability events in the critical portion of the fault. The slip distributions of many small events (small blue circles) are concentrated near the edges of that section around  $x = 50$  km and  $x = 85$  km, while larger events (yellow and orange circles) are concentrated in the central part around  $x = 60$  km. As the small events are more numerous, this creates a non-uniform distribution of the number of events in the critical portion. As shown in Fig. 3(d), there is a bimodal distribution of event number in the critical section of the fault. Most are concentrated around  $x = 85$  km, which constitutes the main active zone in our simulations, with additional concentration near

the boundary between critical section and the SSE patch (around  $x = 50$  km). There is another peak in the event density at the boundary between the SSE patch and seismogenic zone (around  $x = 25$  km), indicating significant interactions between the creeping section in the SSE patch and the earthquakes and tremors generated in our simulation. These results are consistent with the two distinct NVT activity regimes observed in the Guerrero region, with one close to the section of the interface affected by SSE (blue dots on Fig. 1a) and the second (sweet spot, Husker *et al.* 2012) located further down dip (green dots on Fig. 1a). On a broader scale, the simulation reproduces the transition from regular earthquakes to SSE and NVT observed in the area (e.g. Kostoglodov *et al.* 2010; Husker *et al.* 2012). A more detailed comparison between the simulation results and observations is presented in the discussion (Section 4).

### 3.2 Characteristics of the instability events: two different behaviours

As shown in the previous section, the simulated instability events are clustered within two active fault sections separated by an SSE patch without seismicity. A more detailed examination of the characteristics and properties of events with centroids in these two active sections illustrates the fundamental effect of  $\varepsilon_D$  on the transition from earthquakes to NVT in the context on the Mexican subduction zone.

Fig. 4 presents the temporal evolution of seismicity, frequency-size event statistics and average stress in the seismogenic part of the fault with  $\varepsilon_D > 0$  (left panels) and the critical region with  $\varepsilon_D = 0$  (right panels). The seismogenic part of the fault is dominated by large seismic cycles with almost periodic mainshocks associated with background microseismicity (Fig. 4a). We observe a temporal evolution during these seismic cycles involving increasing rates and sometime also increasing magnitudes before the large earthquakes. The associated frequency-size statistics (Fig. 4b) show an overall characteristic distribution with a clear seismicity gap between  $M = 5.3$  and  $M = 6.5$ . The average stress on that fault section (Fig. 4c) has a cyclical structure with large stress drops during the major earthquakes and overall stress increase in between. The stress evolution includes two sudden increases at  $t = 23$  yr and  $t = 42$  yr. The first at  $t = 23$  yr results from the imposed large earthquakes at the bounding patches (regions II and IV in Fig. 1b) to the SW and SE of the computational grid. The second increase at  $t = 42$  yr is due to interactions with the creeping SSE patch.

In contrast, the seismic activity in the critical portion of the fault exhibits a scale-invariant behaviour involving quasi-continuous activity of similar size events with only small statistical fluctuations (Fig. 4d). Note that there is no persisting correlation to the occurrence of the larger events on the seismogenic portion of the fault. The corresponding frequency-size statistics follows the Gutenberg-Richter distribution (Fig. 4e) without the magnitude gap observed for the section with  $\varepsilon_D > 0$ . The temporal evolution of the stress has no cyclical behaviour associated with the large events on this (or the other) fault section, but rather presents small-amplitude fluctuations with scale-invariant character (inset in Fig. 4f). These evolving stress properties indicate that the associated fault section is always close to failure, as expected for a critical behaviour (Fisher *et al.* 1997; Ben-Zion 2012). The differences in the properties of instability events and stress evolution, and the implied greater sensitivity to triggering (see Section 3.5) correspond well to the observed transition from earthquakes to SSE and NVT at the Guerrero section of the Mexican subduction zone.

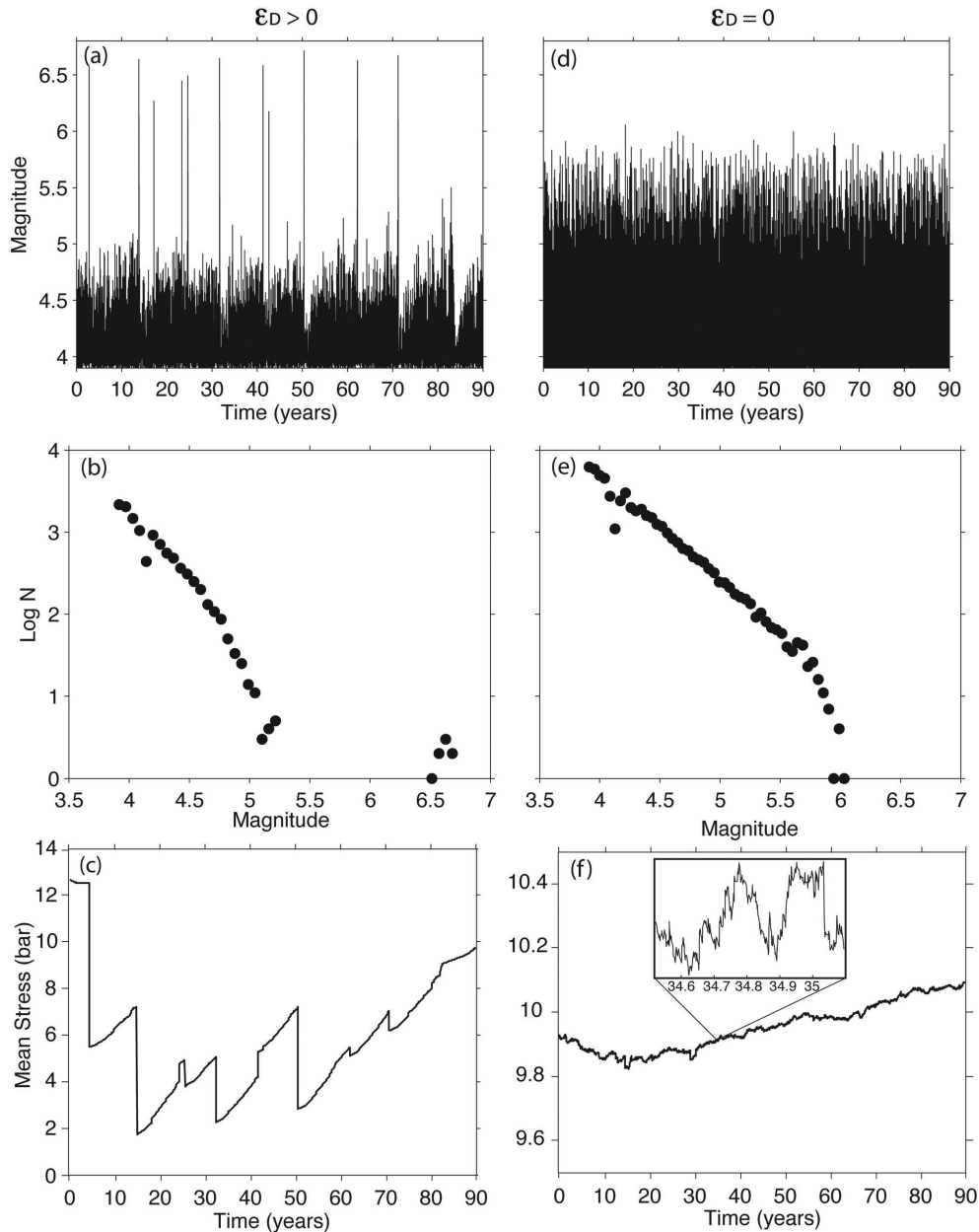


**Figure 4.** Properties of instability events in the seismogenic portion with  $\epsilon_D > 0$  (left panels) and the critical section where  $\epsilon_D = 0$  (right panels). (a, d) Event magnitudes versus time showing large seismic cycles for (a) and almost continuous activity for (d). (b, e) Frequency-size event statistics with characteristic earthquake and Gutenberg–Richter distributions for the seismogenic zone (b) and critical fault section (e). (c, f) Mean stress variations reflecting large earthquakes in the seismogenic zones and small fluctuations in the critical section. The inset in (f) illustrates the fractal nature of the stress variations on the critical section with  $\epsilon_D = 0$ .

The simulated frequency-size distributions are model predictions that cannot yet be compared with observed data due to lack of sufficient earthquake and NVT/LFE catalogues for the Guerrero region. This may change soon given the increasing number of recording stations and the development of new earthquake and LFE detection and location methods (e.g. Frank & Shapiro 2014; Frank *et al.* 2014, 2015a; Ross & Ben-Zion 2014). The effects of the imposed bounding earthquakes are illustrated further in the supplementary Fig. S1. On the seismogenic section with  $\epsilon_D > 0$ , a large event is induced at  $t = 23$  yr and is followed 1.3 yr later by another large event (Fig. S1a). The critical section with  $\epsilon_D = 0$  has induced moderate event at  $t = 23$  yr while maintaining an overall scale-invariant behaviour

(Fig. S1b). The SSE patch sustains at  $t = 23$  yr a sharp increase of the creep slip from 24 cm to 32 cm (Fig. S1c).

Fig. 5 highlights the different nature of the events in the seismogenic and critical sections by showing the slip distributions of several representative events. The seismogenic section sustains regular slip distributions over geometrically compact failure areas (Figs 5b and c). In contrast, the critical fault section has fractal slip distributions on the failure areas with fractal dimension of about 1.8 and multiple disconnected patches that break at the same time (Figs 5d and e). Due to the scale-invariant fluctuations of stress on that fault section (Fig. 4f), the generated slip distributions are not similar to each other but have considerable variability as illustrated by

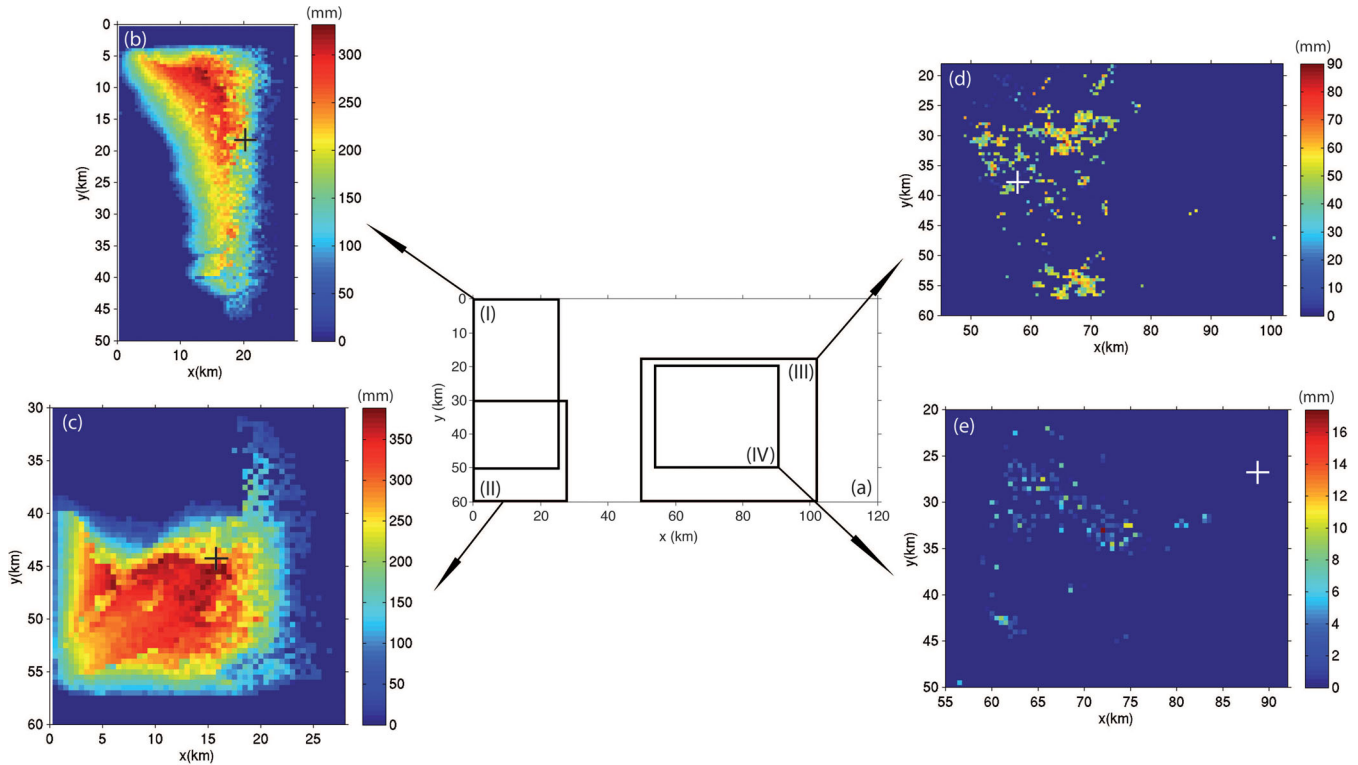


**Figure 5.** Representative examples of slip distributions during instability events on the computational grid. (a) Black rectangle shows the locations of the example slip distributions. (b, c) Slip distributions of events in the seismogenic part of the fault with geometrically compact shapes. (d, e) Slip distributions of events in the critical section of the fault, with fractal shapes consisting of disconnected patches that may correspond to collection of low-frequency earthquakes. The colour scale indicates the slip in millimetres. The black and white crosses (colour change between panels for better visualization) show the hypocentre locations.

the two examples in Figs 5(d) and (e). This behaviour is similar to what is expected for NVT assuming they consist of a succession of LFEs, which break multiple small brittle patches on the subduction interface (Shelly *et al.* 2007).

### 3.3 Creep slip evolution in the SSE patch

The creep slip accumulates continuously on the fault during the simulations, with an approximately linear trend due to the loading associated with the ongoing plate velocity  $V_{pl}$ . In order to examine in detail the variations of creep slip on the section of the fault representing the SSE patch ( $30 < x < 46$  km), we remove a best fitting linear trend from the creep slip data and plot the obtained variations as a function of space and time (Fig. 6).

Fig. 6(a) presents the space-time evolution of the detrended creep slip on the SSE patch for the 90 yr of model evolution. The spatial variations along  $x$  are relatively smooth, with slightly higher values in the central part ( $35 < x < 40$  km) and decreasing creep slip at the edges of the SSE patch. This general behaviour is controlled by the input distribution of  $c(x, y)$  shown in Fig. 2(c), along with the space-time variations of the stress distribution on the fault. We average the variations along the  $x$ -axis to obtain an average time evolution of the creep slip in the SSE patch (Fig. 6b). The results show a complex temporal evolution with both long- and short-term changes during the examined 90 yr. To study the characteristics of that creep slip, we analyze the spectral content of the signal (Fig. 6c) and the temporal changes of different features (Fig. 6d).

The spectral content of the creep slip (Fig. 6c) has four main picks for periods of  $T = 30, 13.2, 5.1$  and  $2.2$  yr. These characteristic periods are visible in Fig. 6(b). The long-term period  $T = 30$  yr is mostly seen for time  $5 < t < 65$  yr, the mid-term period  $T = 13.2$  yr is concentrated at the beginning ( $t < 10$  yr) and at the end ( $t > 65$  yr) of the model evolution, while the short-term variations  $T = 5.1$  yr and  $T = 2.2$  are more distributed in time with less clear temporal clustering. The results are better recognized in Fig. 6(d), which presents the S-transform spectrogram (Stockwell *et al.* 1996) of the average creep slip presented in Fig. 6(b), showing the energy of fluctuations with characteristic time-scale  $T$  in the analyzed signal versus time. The temporal characteristics of the long ( $T = 30$  yr) and intermediate ( $T = 13.2$  yr) variations are indicated in Fig. 6(d) with I, II<sub>1</sub> and II<sub>2</sub>. We do not necessarily attach strong significance to the long-term variations as they may be related to the boundary conditions used in the simulations. We show them to illustrate the possible emergence of long-term temporal patterns due to the interactions of the fault with its surroundings.

The S-transform spectrogram (Fig. 6d) allows a better description of the short-term variations, which are not stable in time. At the beginning of the simulation a clear  $T = 4$  yr variation is visible for time range  $5 < t < 20$  yr (zone III in Fig. 6d). From  $t = 20$  yr to  $t = 35$  yr, we observed only small timescale variations with periods of about a year or less (Figs 6b and d). At  $t = 35$  yr, variations with  $T \approx 5$  yr start and continue up to  $t = 58$  yr (zone IV in Fig. 6d). This 20 yr long activity overlap with the  $T = 2.2$  yr variations around  $t = 35$  yr and  $t = 54$  yr (zones V<sub>1</sub> and V<sub>2</sub> in Fig. 6d). From  $t = 58$  yr to  $t = 73$  yr there is a second quiet interval with only

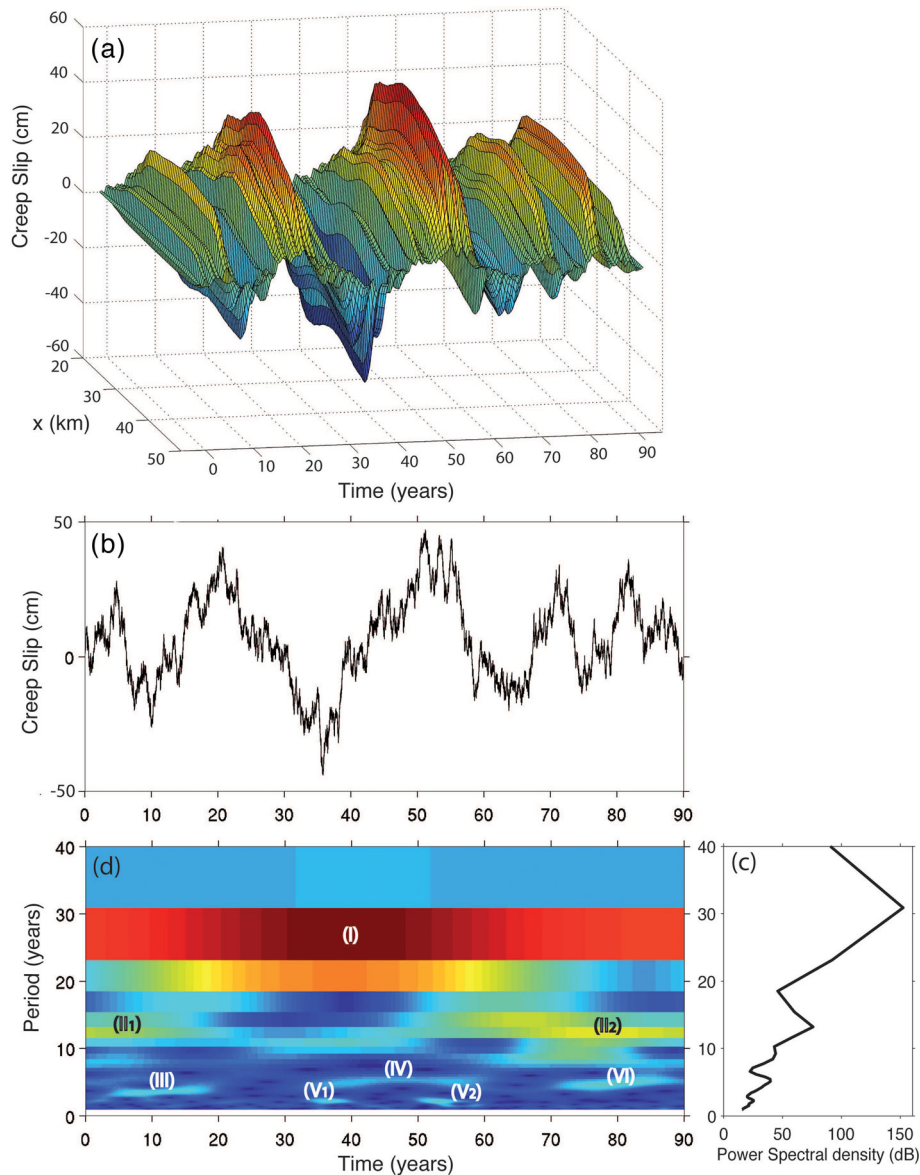


**Figure 6.** (a) Space–time evolution of the creep slip on the SSE patch ( $20 < x < 50$  km). (b) Temporal evolution of the average creep slip along the  $x$ -axis on the SSE patch. (c) Power spectral density of (b). (d) S-transform spectrogram of (b). The colour indicates the amplitude of the S-transform. The numbers in black and white refer to zones discussed in the text.

small-scale variations. Finally, for  $t > 73$  yr we observed again the  $T \approx 5.1$  yr variations (zone VI in Fig. 6d). This analysis highlights the variability of the simulated creep slip and shows that the simple model is producing a complex temporal evolution that is suspected for natural fault systems.

While the model results include long-term evolution that cannot be compared with actual data, the short-term variations resemble the four observed SSEs in the Guerrero segment. The creep slip variations with  $T = 5.1$  yr and  $T = 4$  yr can be compared with the patterns associated with the recorded SSEs in 1998, 2002, 2006 and 2009–2010, with a recurrence time of about 4 yr (e.g. Cotte *et al.* 2009; Walpersdorf *et al.* 2011; Radiguet *et al.* 2012). This is better illustrated in Fig. 7, which compares two 15 yr intervals (Figs 7a and b) extracted from Fig. 6(b) with a detrended GPS time series recorded at station CAYA (see location in Fig. 1a) between 1997 and 2011 (Fig. 7c). The two selected 15 yr intervals correspond to zones III (Fig. 7a) and VI (Fig. 7b) of Fig. 6(d), where  $T =$

4–5 yr variations are observed. The different amplitudes of the model creep slip and observed GPS data are related to the fact that the former occur on the fault interface while the latter are recorded at the surface. Inversions of the surface GPS data for the 2002, 2006 and 2009–2010 SSEs led to mean slip values at the interface (Radiguet *et al.* 2012) between 7.7 and 9.4 cm, with maximum slip up to 20 cm, which is close to our simulation results.

We note that although the duration of cycles is similar in the simulation and observations ( $\sim 4$ –5 yr), the SSEs appear to be more rapid in nature; about 6 months in the GPS time series versus a couple of model years (Fig. 7). This reflects a more continuous sliding of the model SSE patch compared to a more transient character of SSE in the natural fault system. The creep slip in our simulation also has more apparent complexity with additional small scale variations compare to the GPS data. The comparison for small amplitude fluctuations is made difficult by the limited resolution of the observations. Additional comparisons between the simulated creep

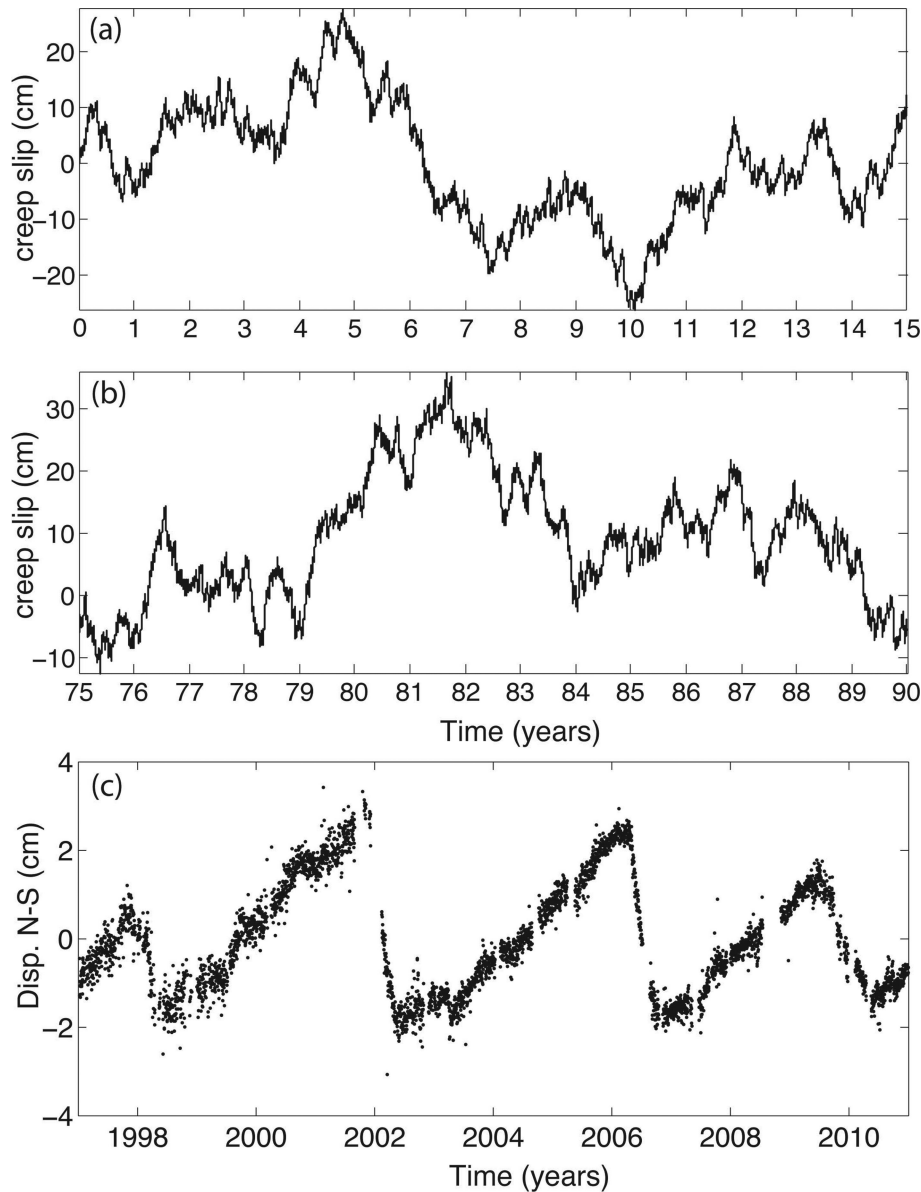


**Figure 7.** (a) Evolution of average creep slip variations on the SSE patch for a 15 yr interval corresponding to zones III of Fig. 6(d). (b) Same as (a) for another example of 15 yr interval corresponding to zones VI of Fig. 6(d). (c) Detrended north–south GPS measurements recorded at CAYA station (see Fig. 1) between 1997 and 2011.

slip and GPS time series recorded at station IGUA and MEZC are provided in the supplementary Fig. S2, which highlights on a 2-yr time interval the complexity of short-term cycles in the model results and their similarities with the overall smoother visual aspect of GPS time series.

### 3.4 Differences between hypocentre and centroid locations

As mentioned in Section 3.2, the slip distributions of the events in the critical section of the fault show multiple small brittle patches that break in a single event in a similar way to LFEs within tremors (Shelly *et al.* 2007). In this section we discuss the relations between hypocentre and centroid locations of different events in different fault sections in relation to the creep evolution. Fig. 8 shows the absolute distances between the centroids and hypocentre locations:  $|x_{\text{centroid}} - x_{\text{hypocentre}}|$  versus hypocentre locations along the  $x$ -axis in relation to the evolving creep in the SSE patch. We observe

that large values of  $|x_{\text{centroid}} - x_{\text{hypocentre}}|$  are concentrated in three sections: (1) on the left edge of the SSE patch in the seismogenic zone around  $x = 25$  km, (2) on the right edge of the SSE patch up to the start of  $\varepsilon_D = 0$  ( $46 < x < 60$  km) and (3) the critical region with  $x > 75$  km. Events initiated in these regions have, on average, large slip away from the hypocentre locations.

To compare these events with the creep slip evolution in the SSE patch ( $30 < x < 46$  km), we use a threshold value for  $|x_{\text{centroid}} - x_{\text{hypocentre}}|$  of 15 km and time window of 4 yr. The basic aspects of the results do not change significantly for threshold values in the range 5–20 km and time windows between 2 and 6 yr. For threshold value above 20 km and/or time window below 2 yr the number of events is not sufficient for analysis. Results associated with  $|x_{\text{centroid}} - x_{\text{hypocentre}}| < 5$  km are common also for regular earthquakes and time windows over 6 yr mix events of different deformation phases.

Figs 8(b)–(d) show the temporal evolution of the number of events (black curves) and average creep slip (red curves) over the SSE

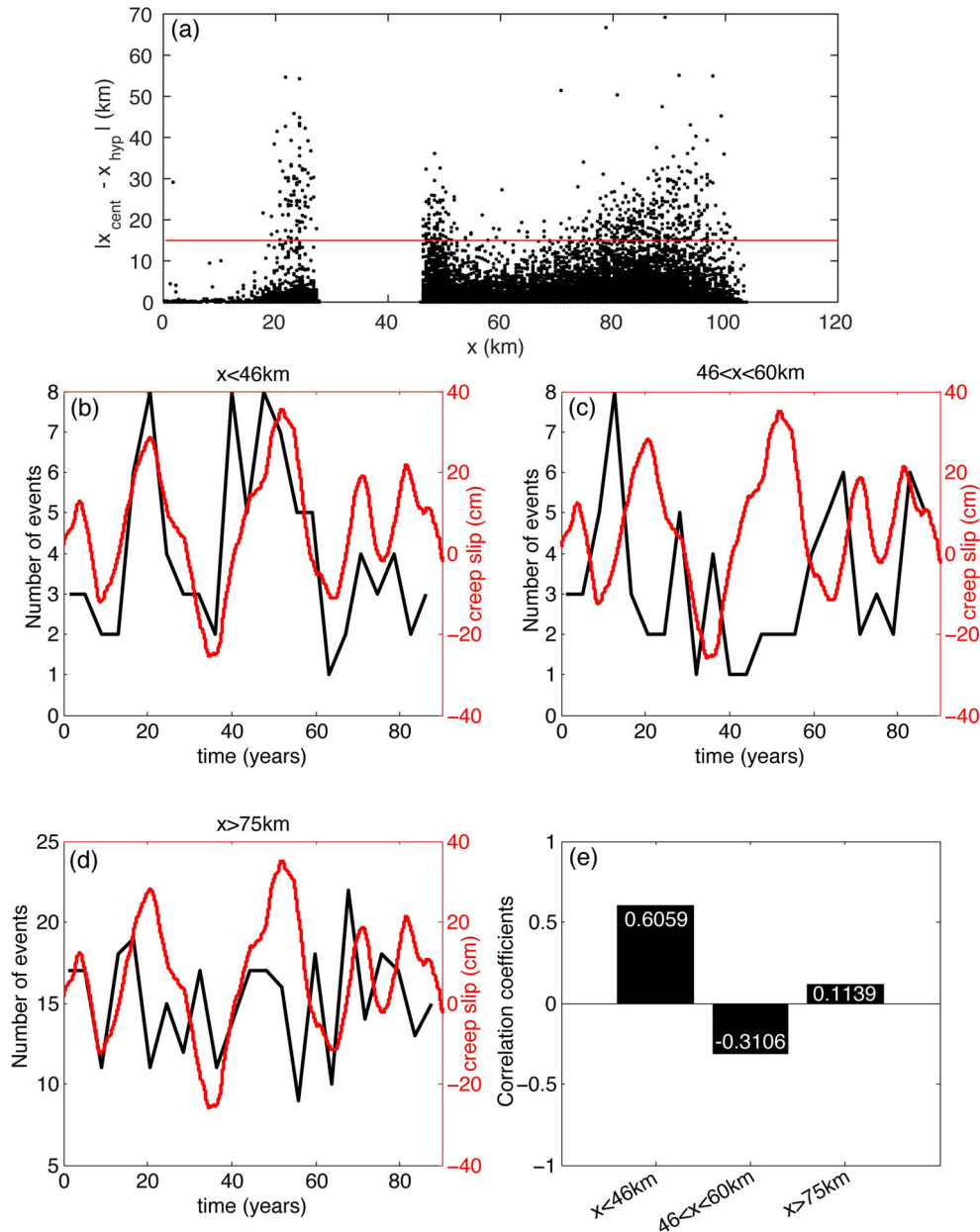


**Figure 8.** (a) Differences  $|x_{\text{centroid}} - x_{\text{hypocentre}}|$  between centroids and hypocentres of slip events versus hypocentre locations. The red horizontal line indicates a threshold  $|x_{\text{centroid}} - x_{\text{hypocentre}}| = 15$  km used for the results presented in subsequent panels. (b–d) Temporal variations of events with  $|x_{\text{centroid}} - x_{\text{hypocentre}}| \geq 15$  km (black curves) and average creep slip over the SSE patch ( $30 < x < 46$  km) in 4-yr time windows for event groups with the following hypocentre locations: (b)  $x < 46$  km, (c) the region  $46 < x < 60$  km between the SSE patch and start of  $\varepsilon_D = 0$ , (d) the critical region  $x > 75$  km. (e) Correlation coefficients between the changes of event numbers and creep slip evolution in panels (b–d).

patch in 4-yr time windows. Fig. 8(e) summarizes the correlation coefficients between these two curves for the three sections. We observe a clear correlation between the creep evolution and the number of events in the regular seismogenic zone (Fig. 8b) with a coefficient of correlation above 0.6 (Fig. 8e). At the opposite side of the SSE patch, for  $46 < x < 60$  km (Fig. 8c), we observe a weak anti-correlation between the slip instability events and the creep evolution. Both of these patterns indicate a close control of events with large separation between their centroids and hypocentres by the temporal evolution of the creep in the SSE patch. In contrast, the events in the critical section ( $x > 75$  km) with scale-invariant stress fluctuations, fractal slip distributions and ongoing critical failure process have little correlation with the creep evolution in the SSE

patch (Fig. 8e) or large earthquakes in the seismogenic zone (Ben-Zion 2012). A comparison between these model predictions and observations in the Guerrero region is presented in the discussion (Section 4).

### 3.5 Triggering by seismic waves

As mentioned, NVT have higher susceptibility to triggering than regular earthquakes. Zigone *et al.* (2012) showed that both NVT and SSE were triggered in the Guerrero region by the Mw 8.8 2010 Maule earthquake. In this section we analyze triggering of NVT and creep events by seismic waves in the model simulations. The

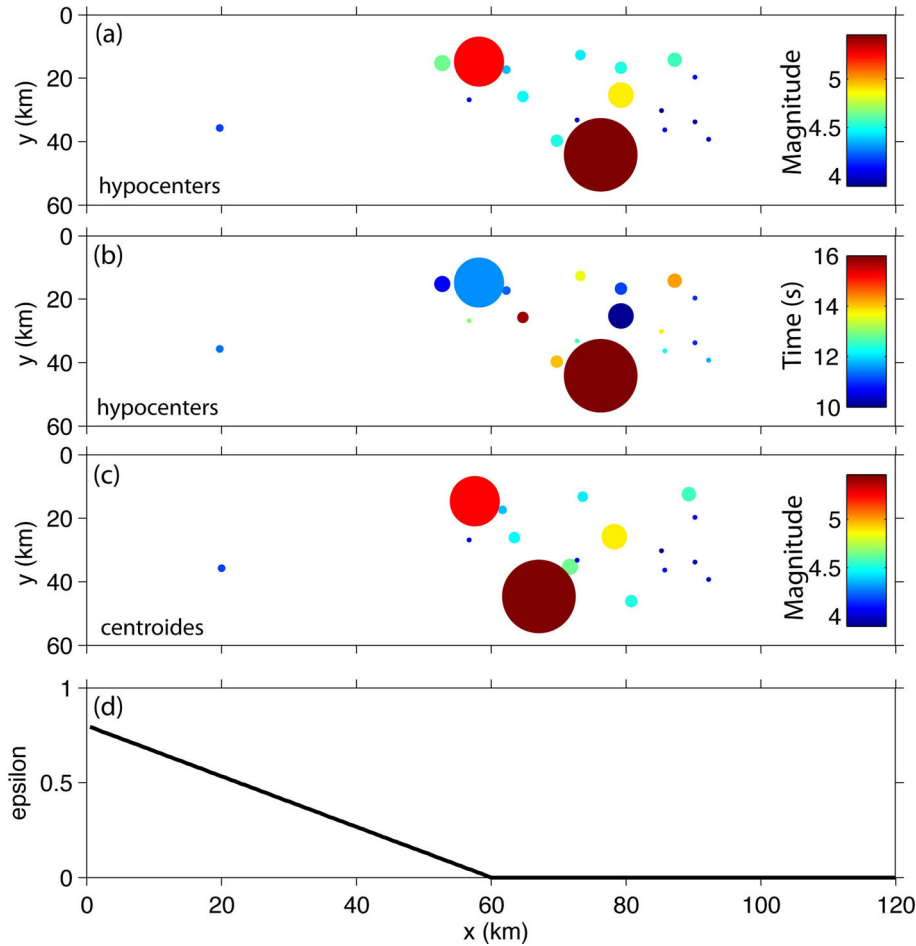


**Figure 9.** Example results for a triggering sequence. (a) Hypocentres of triggered instability events with circle size proportional to the failure area of the events and colours indicating magnitudes. (b) Similar to (a) with colours indicating time in seconds. (c) Similar to (a) for centroids of the triggered instability events. (d) Distribution of  $\epsilon_D$  along the  $x$ -axis.

triggering is implemented by adding periodic stress oscillations to the regular tectonic loading on each cell  $(i, j)$  of the computational grid. This periodic loading is given by

$$\tau_{\text{wave}}(i, j, t) = A \sin\left(\frac{2\pi}{T}t\right), \quad (4)$$

where  $t$  is time. The amplitude and period of the wave are assumed  $A = 0.01$  MPa and  $T = 30$  s. The triggering sequence has a total duration of 15 min during which we use a computation time step of 0.1 s.

The main consequence of a triggering sequence is the sudden increase by a factor of 10 in the number of instability events on the fault. When no triggering waves are applied there are about 2 events per day on average in the critical fault section. In contrast, there are about 20 to 35 triggered events in each 15 min triggering sequence. Fig. 9 shows example results from one triggering sequence. Almost all hypocentres of the triggered events are located in the critical part of the fault (Fig. 9a), reflecting that this fault section is always close to failure. The temporal evolution of the hypocentres of triggered events (Fig. 9b) has no clear migration patterns as expected for critical processes (Ben-Zion 2012). As shown by the distribution of centroids in Fig. 9(c), the slip of the higher magnitude triggered events is concentrated close to  $x = 60$  km where  $\epsilon_D$  becomes zero. This behaviour is observed for all triggering sequences and indicates

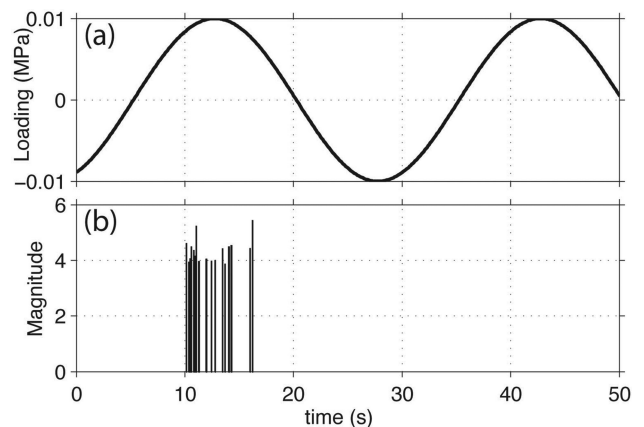


**Figure 10.** (a) Small oscillatory component added to the tectonic loading to simulate waves from a large remote earthquake. (b) Corresponding occurrence of instability events on the fault.

interaction between simulated NVT and teleseismic earthquakes in the transition zone where  $\epsilon_D$  approaches zero.

Fig. 10 presents the temporal correlation between the triggering oscillation (top panel) and the triggered instability events (bottom panel). In this simulated case, all the events occur during the first cycle, in contrast to the observations of Zigone *et al.* (2012) of

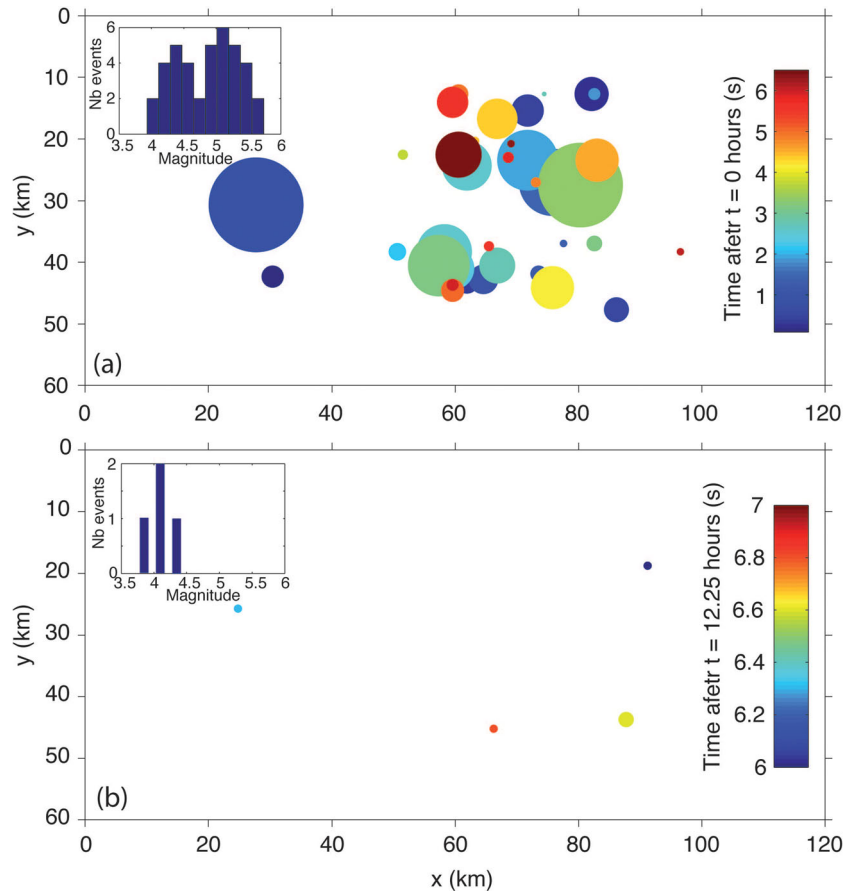


**Figure 11.** Example results for multiple triggering cycles. (a) Hypocentre location, rupture area (circle size) and time after the start of the sequence (colour) of 40 triggered event in the first cycle. The inset shows the magnitude distribution of the events. (b) Same as (a) for the four events triggered in the second cycle. The time in (b) is in seconds after  $t = 12.25$  hr in the triggering sequence.

triggered NVT also by multiple strain oscillations produced by the long period surface waves of the Maule earthquake. In the case of the Maule earthquake, the multiple NVT triggering was likely associated with the simultaneous triggering of slow slip that may enhanced the tremor activity as the multiple surface waves reached Guerrero (Zigone *et al.* 2012). In our model, the lack of triggering following the first oscillation is related to the short time scale of the triggering sequences (15 min), which does not allow in the absence of triggered SSE enough stress redistribution on the relatively large used cell size. Possible reasons for the lack of SSE triggering are addressed in the discussion section.

To compensate for the relatively large cell size and the short triggering sequences used in this study, we simply allow ‘more loading time’ by adding oscillatory waves with same parameters as in eq. (3), 12 hr after the initial triggering sequence (Fig. 11). In this case, a total of 44 events are triggered, with 40 triggered in the first application of oscillatory stress and 4 in the second (Fig. 11a). The first sequence has a bimodal magnitude distribution with clusters around  $M = 4.4$  and  $M = 5.1$ , while the magnitudes in the second sequence are overall lower and scattered (insets in Fig. 11a). The hypocentre distributions of the triggered NVT events in the first and second application of triggering waves (Figs 11a and b) are similar to that generated by the previous triggering example (Fig. 9), with most of the events in the critical fault portion. Except for the sudden change in the creep slip associated with the ruptures of the bounding earthquakes patches (regions II and IV in Fig. 1b) illustrated in Fig. S1c, the simulation results do not show SSE triggering, in contrast to

the observations of Zigone *et al.* (2012). Some interactions between the slow slip patch, added oscillatory stresses and triggered NVT events may exist in the used model realization, but depend of the specific timing of the sequence. We also note that reducing the cell size will increase the strength of interaction between different fault sections, and may increase the likelihood of triggered SSEs. Additional simulations with considerably lower cell size (and other model modifications) may be attempted in future work.

#### 4 DISCUSSIONS AND CONCLUSIONS

We simulate and analyze 90 yr of brittle and creep slip events on a planar interface governed by space-varying static/kinetic friction and dislocation creep in elastic solid. The geometrical, loading and rheological properties are tailored to represent the Guerrero subduction zone, Mexico. The model produces more than 70 000 instability events that are clustered within two active fault sections separated by an SSE patch without seismicity (Fig. 3). This hypocentre distribution delineates three distinct fault sections, referred to as seismogenic zone, SSE patch and critical part, that reproduce the transitions from regular earthquakes to slow creep events and NVT observed in the Guerrero area (e.g. Payero *et al.* 2008; Kostoglodov *et al.* 2010; Husker *et al.* 2012). The southern section corresponds to a typical seismogenic zone with moderate local earthquakes and background microseismicity as in the natural fault system. Most of the simulated microseismicity is concentrated around  $x = 20$  km, at

the edge of the SSE patch, suggesting a link between creep events and microseismicity. This is demonstrated on Fig. 8(b), which shows a clear correlation between the creep slip and the temporal evolution of the events with large distances between their centroids and hypocentres. Similar spatio-temporal correlations may be reflected in the Guerrero area by high seismicity rates associated with the 1998, 2002 and 2006 SSEs (Liu *et al.* 2007). We note that the observational results cover only magnitudes above 4.5 due to limited data resolution (Liu *et al.* 2007). Future analysis of more complete data may show better the link between SSEs and microseismicity at the lower end of the seismogenic zone.

The model SSE patch creates a bimodal distribution of the number of NVT in the critical section illustrated in Fig. 3(d). The peak around  $x = 85$  km is present also in model realizations with other distributions of  $c(x, y)$  not generating an SSE patch (dashed line in Fig. 2c). However, the peak at  $x = 50$  km appears only when the assumed  $c(x, y)$  distribution includes a region corresponding to the SSE patch (Fig. 2c solid line), indicating a strong relation between the spatial properties of the model SSE and NVT. This pattern is similar to what is observed by Husker *et al.* (2012) with two distinct NVT activity regimes in Guerrero. The updip portion, closer to the seismogenic zone, has episodes of NVT related to the transient stresses produced by the SSE. This has been clearly established for the 2006 SSE with triggered NVT epicentres found to be collocated with the SSE sliding front (Husker *et al.* 2012; Rivet *et al.* 2014). In addition, Zigone *et al.* (2012) showed a temporal link between the GPS displacement rate and the NVT activity in Mexico, suggesting a close control of some tremor activity by the slow slip history outside the periods of the large SSEs. In contrast, the downdip section closer to the stable sliding portion has almost continuous NVT activity, with higher energy NVT episodes every several months (Husker *et al.* 2012). The model results reproduce well this variability and suggest a physical link between creep slip and NVT in Guerrero related to the shear stress accumulation at the tip of the SSE patch.

The transition from earthquake to NVT-type events is controlled by the decrease of the strength-change parameter  $\varepsilon_D$  along the fault. When  $\varepsilon_D > \varepsilon_c \sim 0$ , the instability events have classical properties of regular earthquakes, with seismicity dominated by large seismic cycles associated with large stress drops and an overall characteristic frequency-size distribution. In contrast, the portion with near-zero  $\varepsilon_D$  produces unstable events that are part of a critical depinning transition of the interface (Ben-Zion 2012). These events have scale-invariant properties with quasi-continuous activity, fractal slip and stress distributions on the interface, and Gutenberg–Richter frequency-size statistics. The physical processes responsible for the transition is  $\varepsilon_D$  are not modelled explicitly. Due to the subhorizontal subduction interface, the temperature gradient is small along the Guerrero segment (Manea & Manea 2011), and cannot explain alone the changes responsible for the drop of the coupling reported by Radiguet *et al.* (2012). The presence of high fluid pressure at some sections may decrease the normal stress and lead to ongoing stable sliding. Fluids may also facilitate fast healing that can produce effectively small  $\varepsilon_D$  corresponding to criticality (Ben-Zion 2012).

The slip distributions of NVT model events show large variability and fractal character with multiple patches that break simultaneously (Figs 5c and d). Such a behaviour is expected for NVT events that consist of a succession of LFEs (Shelly *et al.* 2007). The simulation results are consistent with multiple LFEs of various size that together creates NVT along the model section  $46 < x < 100$  km. Frank *et al.* (2013) observed 15 families of LFEs within the tremors

recorded in the Mexico's 'sweet spot' (Husker *et al.* 2012) and located at the subduction interface. The stacked focal mechanism of these LFEs is represented by a single shallow-thrusting double-couple consistent with the overall stress release in the Mexican subduction zone (Frank *et al.* 2013). Our model results are consistent with these observations and suggest that each of the LFE families is related to a particular fault patch that breaks in a critical fashion regularly due to the plate loading. The NVT–LFE patches in our model are not limited to the downdip section close to the continuous sliding portion of the fault but also exist in the updip section close to the SSE patch (around  $x = 50$  km). This 'model prediction' has been recently confirmed by Frank *et al.* (2014), who observed discrete episodes of LFE in the region associated with SSE and a near-continuous activity observed in the downdip 'sweet spot' NVT region as in our simulation results.

The analysis of hypocentre locations and centroids of slip distributions associated with individual events indicates that the events with  $|x_{\text{centroid}} - x_{\text{hypocentre}}| \geq 15$  are located at both edges of the SSE patch and in the critical section of the fault (Fig. 8a). A comparison with the creep slip evolution shows that events located at the edges of the SSE patch are affected strongly by the temporal evolution of the creep in the SSE patch, while events in the critical section are influenced primarily by the ongoing critical sliding process and fractal character of the stress and slip events (Figs 8b–d). These results are consistent with the recent observations of Frank *et al.* (2014) that LFEs in the downdip portion of the interface (sweet spot) tend to migrate over 30–60 km. Such migrations imply large spatial extent of the NVT episodes along the subduction interface as in our simulation results. Frank *et al.* (2014) did not observe migrations outside the sweet spot in Mexico. However, our model results suggest that improved detection methods may reveal LFEs migrations in regions close to the SSE patch. As in our simulation results, such migrations may be linked to the slow slip evolution.

Model simulations with small added stress oscillations are used to examine the triggering of NVT by large remote earthquakes. The first oscillation of the added stresses increases the number of instability events in the critical portion by a factor of 10 (Fig. 9), reflecting the fact that this fault section is always close to failure. Additional triggering sequence is generated by added stress oscillations that is delayed (by 12 hr in the used model realization) to compensate for the relatively coarse grid and other model approximations. These simulated results reproduce the main observed aspects of tremor triggering in the Mexican NVT sweet spot by teleseismic waves of the Mw 8.8 Maule earthquake (Zigone *et al.* 2012). Another illustration of the key role played by criticality on triggering susceptibility is given by Ben-Zion (2012) with small added seasonal stress oscillations.

The present model employs a power-law dislocation creep to describe stable sliding along the interface (Ben-Zion 1996). The small added oscillatory stress that represents waves from a large distant earthquake does not trigger a model SSE, in contrast to the observations of Zigone *et al.* (2012). The triggering of SSE in Guerrero occurred at a time inferred by Zigone *et al.* (2012) to be associated with particularly high stress on the subduction interface because of the previous events history. We did not find example of similar behaviour in the simulated results, although some tests with small added oscillatory stress at a time of high stress on the SSE patch produced enhanced creep during the triggering sequence. A creep law that includes a weakening of the creep coefficient with slip may produce occasional triggered SSE events similar to the observations of Zigone *et al.* (2012). Such a slip-dependent

creep law is consistent with inferences associated with combined observations and inversion results of Radiguet *et al.* (2011) and Maury *et al.* (2014).

Fig. 7 highlights the similarity of the modelled creep slip with the observed GPS time series recorded in Mexico, with similar variations over a period around 3–5 yr. Our simulations include additional features that go beyond the existing observations. The model results show short-term variations with recurrence times of weeks to a few days. Such short-term SSE have been documented in Japan, where more precise instruments (e.g. strainmeters and/or tiltmeters) demonstrated the presence of slow slip episodes with duration and recurrence time ranging from a few days to a few tens of days (e.g. Obara 2011, and reference therein). In Mexico, several studies also suggested the presence of smaller transient episodes with duration of a few weeks based on advanced GPS processing methods (Vergnolle *et al.* 2010) and on NVT activities (Husker *et al.* 2012; Rivet *et al.* 2014; Frank *et al.* 2015b).

Our model results also include long-term evolution of creep slip over time scales of 15 to 30 yr (Fig. 6). In the employed model realization, these are characterized by creep variations over  $T \sim 5$  yr followed by quiet intervals having only short transients with  $T < 1$  yr. Such changes including potential quiet intervals without large SSE can have an important impact on the deformation process, since any decreases in the SSE rate or a lack of SSE during a certain time interval may advance the occurrence of the next large rupture. This scenario highlights the need to develop a more detailed numerical model that assimilates additional available information and includes history-dependent rheological properties that account for more feedback mechanisms between the different slip modes on the fault. This may be the subject of a follow up work.

## ACKNOWLEDGEMENTS

We thank Diane Rivet, Paul Johnson, William Frank and Christophe Voisin for useful discussions. The study was funded by the Earthquake Hazards Program of the USGS (grant G12AP20067) and the Agence Nationale de la Recherche, France (contract RA0000CO69 G-GAP). The paper benefited from comments by Olaf Zielke, Allen Husker and editor Saskia Goes.

## REFERENCES

- Anderson, J.G., Singh, S.K., Espindola, J.M. & Yamamoto, J., 1989. Seismic strain release in the Mexican subduction thrust, *Phys. Earth planet. Inter.*, **58**, 307–322.
- Ben-Zion, Y., 1996. Stress, slip and earthquakes in models of complex single-fault systems incorporating brittle and creep deformations, *J. geophys. Res.*, **101**, 5677–5706.
- Ben-Zion, Y., 2008. Collective behavior of earthquakes and faults: continuum-discrete transitions, evolutionary changes and corresponding dynamic regimes, *Rev. Geophys.*, **46**, RG4006, doi:10.1029/2008RG000260.
- Ben-Zion, Y., 2012. Episodic tremor and slip on a frictional interface with critical zero weakening in elastic solid, *Geophys. J. Int.*, **189**, 1159–1168.
- Ben-Zion, Y. & Rice, J.R., 1993. Earthquake failure sequences along a cellular fault zone in a three-dimensional elastic solid containing asperity and nonasperity regions, *J. geophys. Res.*, **98**, 14 109–14 131.
- Ben-Zion, Y. & Rice, J.R., 1995. Slip patterns and earthquake populations along different classes of faults in elastic solids, *J. geophys. Res.*, **100**, 12 959–12 983.
- Ben-Zion, Y. & Zhu, L., 2002. Potency-magnitude Scaling Relations for Southern California Earthquakes with  $1.0 < M_L < 7.0$ , *Geophys. J. Int.*, **148**, F1–F5.
- Ben-Zion, Y., Dahmen, K.A. & Uhl, J.T., 2011. A unifying phase diagram for the dynamics of sheared solids and granular materials, *Pure appl. Geophys.*, **168**, 2221–2237.
- Ben-Zion, Y., Eneva, M. & Liu, Y., 2003. Large earthquake cycles and intermittent criticality on heterogeneous faults due to evolving stress and seismicity, *J. geophys. Res.*, **108**(B6), 2307, doi:10.1029/2002JB002121.
- Beroza, G. & Ide, S., 2011. Slow earthquakes and nonvolcanic tremor, *Annu. Rev. Earth Planet. Sci.*, **39**, 271–296.
- Brown, K.M., Tryon, M.D., DeShon, H.R., Dorman, L.M. & Schwartz, S.Y., 2005. Correlated transient fluid pulsing and seismic tremor in the Costa Rica subduction zone, *Earth planet. Sci. Lett.*, **238**(1–2), 189–203.
- Burlini, L., Di Toro, G. & Meredith, P., 2009. Seismic tremor in subduction zones: rock physics evidence, *Geophys. Res. Lett.*, **36**, L08305, doi:10.1029/2009GL037735.
- Cotte, N., Walpersdorf, A., Kostoglodov, V., Vergnolle, M., Santiago, J.-A., Manighetti, I. & Campillo, M., 2009. Anticipating the next large silent earthquake in Mexico, *EOS, Trans. Am. geophys. Un.*, **90**(21), 181–182.
- Dahmen, K. & Ben-Zion, Y., 2009. The physics of jerky motion in slowly driven magnetic and earthquake fault systems, in *Encyclopedia of Complexity and System Science*, Vol. 5, pp. 5021–5037, ed. Meyers, R., Springer.
- Dahmen, K.A., Ben-Zion, Y. & Uhl, J.T., 2009. A micromechanical model for deformation in disordered solids with universal predictions for stress-strain curves and related avalanches, *Phys. Rev. Lett.*, **102**, 175501, doi:10.1103/PhysRevLett.102.175501.
- Demets, C., Gordon, R.G., Argus, D.F. & Stein, S., 1994. Effect of recent revisions to the geomagnetic reversal time-scale on estimates of current plate motions, *Geophys. Res. Lett.*, **21**(20), 2191–2194.
- Fisher, D.S., Dahmen, K., Ramanathan, S. & Ben-Zion, Y., 1997. Statistics of Earthquakes in Simple Models of Heterogeneous Faults, *Phys. Rev. Lett.*, **78**, 4885–4888.
- Frank, W.B. & Shapiro, N.M., 2014. Automatic detection of low-frequency earthquakes (LFEs) based on a beam formed network response, *Geophys. J. Int.*, **197**(2), 1215–1223.
- Frank, W.B., Shapiro, N.M., Husker, A.L., Kostoglodov, V., Bhat, H.S. & Campillo, M., 2015a. Along-fault pore-pressure evolution during a slow-slip event in Guerrero, Mexico, *Earth planet. Sci. Lett.*, doi:10.1016/j.epsl.2014.12.051.
- Frank, W.B., Shapiro, N.M., Husker, A.L., Kostoglodov, V., Romanenko, A. & Campillo, M., 2014. Using systematically characterized low-frequency earthquakes as a fault probe in Guerrero, Mexico, *J. geophys. Res.*, **119**(10), 7686–7700.
- Frank, W.B., Shapiro, N.M., Kostoglodov, V., Husker, A.L., Campillo, M., Payero, J.S. & Prieto, G.A., 2013. Low-frequency earthquakes in the Mexican Sweet Spot, *Geophys. Res. Lett.*, **40**, doi:10.1002/grl.50561.
- Frank, W.B., Radiguet, M., Rousset, B., Shapiro, N.M., Husker, A.L., Kostoglodov, V., Cotte, N. & Campillo, M., 2015b. Uncovering the geodetic signature of silent slip through repeating earthquakes, *Geophys. Res. Lett.*, doi:10.1002/2015GL063685.
- Ghosh, A., Vidale, J.E., Peng, Z., Creager, K.C. & Houston, H., 2009. Complex nonvolcanic tremor near Parkfield, California, triggered by the great 2004 Sumatra earthquake, *J. geophys. Res.*, **114**, B00A15, doi:10.1029/2008JB006062.
- Husker, A.L., Kostoglodov, V., Cruz-Atienza, V.M., Legrand, D., Shapiro, N.M., Payero, J.S., Campillo, M. & Huesca-Perez, E., 2012. Temporal variations of non-volcanic tremor (NVT) locations in the Mexican subduction zone: Finding the NVT sweet spot, *Geochem. Geophys. Geosyst.*, **13**, Q03011, doi:10.1029/2011gc003916.
- Kostoglodov, V., Husker, A., Shapiro, N.M., Payero, J.S., Campillo, M., Cotte, N. & Clayton, R., 2010. The 2006 slow slip event and nonvolcanic tremor in the Mexican subduction zone, *Geophys. Res. Lett.*, **37**, L24301, doi:10.1029/2010gl045424.
- Kostoglodov, V., Singh, S.K., Santiago, J.A., Franco, S.I., Larson, K.M., Lowry, A.R. & Bilham, R., 2003. A large silent earthquake in the Guerrero seismic gap, Mexico, *Geophys. Res. Lett.*, **30**(15), 1807, doi:10.1029/2003GL017219.

- Liu, Y. & Rice, J.R., 2009. Slow slip predictions based on granite and gabbro friction data compared to GPS measurements in northern Cascadia, *J. geophys. Res.*, **114**, B09407, doi:10.1029/2008JB006142.
- Liu, Y., Rice, J. & Larson, K., 2007. Seismicity variations associated with aseismic transients in Guerrero, Mexico, 1995–2006, *Earth planet. Sci. Lett.*, **262**(3–4), 493–504.
- Manea, V.C. & Manea, M., 2011. Flat-slab thermal structure and evolution beneath central Mexico, *Pure Appl. Geophys.*, **168**(8–9), 1475–1487.
- Maury, J., Aochi, H. & Radiguet, M., 2014. Fault constitutive relations inferred from the 2009–2010 slow slip event in Guerrero, Mexico, *Geophys. Res. Lett.*, **41**, doi:10.1002/2014GL060691.
- Mehta, A.P., Dahmen, K.A. & Ben-Zion, Y., 2006. Universal mean moment rate profiles of earthquake ruptures, *Phys. Rev. E.*, **73**, 056104, doi:10.1103/PhysRevE.73.056104.
- Nishenko, S. & Singh, S.K., 1987. Conditional Probabilities for the recurrence of large and great interplate earthquakes along the Mexican subduction zone, *Bull. seism. Soc. Am.*, **77**(6), 2095–2114.
- Obara, K., 2002. Nonvolcanic deep tremor associated with subduction in southwest Japan, *Science*, **296**(5573), 1679–1681.
- Obara, K., 2011. Characteristics and interactions between non-volcanic tremor and related slow earthquakes in the Nankai subduction zone, southwest Japan, *J. Geodyn.*, **52**, 229–248.
- Obara, K., Hirose, H., Yamamizu, F. & Kasahara, K., 2004. Episodic slow slip events accompanied by non-volcanic tremors in southwest Japan subduction zone, *Geophys. Res. Lett.*, **31**(23), L23602, doi:10.1029/2004GL020848.
- Obara, K., Matsuzawa, T., Tanaka, S., Kimura, T. & Maeda, T., 2011. Migration properties of non-volcanic tremor in Shikoku, southwest Japan, *Geophys. Res. Lett.*, **38**, L09311, doi:10.1029/2011GL047110.
- Ohta, Y., Freymueller, J.T., Hreinsdottir, S. & Suito, H., 2006. A large slow slip event and the depth of the seismogenic zone in the south central Alaska subduction zone, *Earth planet. Sci. Lett.*, **247**(1–2), 108–116.
- Outerbridge, K.C. *et al.*, 2010. A tremor and slip event on the Cocos-Caribbean subduction zone as measured by a global positioning system (GPS) and seismic network on the Nicoya Peninsula, Costa Rica, *J. geophys. Res.*, **115**, B10408, doi:10.1029/2009jb006845.
- Pardo, M. & Suarez, G., 1995. Shape of the subducted Rivera and Cocos plates in southern Mexico - seismic anti tectonic implications, *J. geophys. Res.*, **100**(B7), 12 357–12 373.
- Payero, J.S., Kostoglodov, V., Shapiro, N., Mikumo, T., Iglesias, A., Perez-Campos, X. & Clayton, R.W., 2008. Nonvolcanic tremor observed in the Mexican subduction zone, *Geophys. Res. Lett.*, **35**(7), L07305, doi:10.1029/2007gl032877.
- Peng, Z. & Gombert, J., 2010. An integrative perspective of coupled seismic and aseismic slow slip phenomena, *Nature Geosci.*, **3**, 599–607.
- Peng, Z., Vidale, J.E., Wech, A.G., Nadeau, R.M. & Creager, K.C., 2009. Remote triggering of tremor along the San Andreas Fault in central California, *J. geophys. Res.*, **114**, B00A06, doi:10.1029/2008JB006049.
- Perez-Campos, X. *et al.*, 2008. Horizontal subduction and truncation of the Cocos Plate beneath central Mexico, *Geophys. Res. Lett.*, **35**(18), L18303, doi: 10.1029/2008gl035127.
- Peterson, C.L. & Christensen, D.H., 2009. Possible relationship between nonvolcanic tremor and the 1998–2001 slow slip event, south central Alaska, *J. geophys. Res.*, **114**, B06302, doi:10.1029/2008jb006096.
- Radiguet, M., Cotton, F., Vergnolle, M., Campillo, M., Valette, B., Kostoglodov, V. & Cotte, N., 2011. Spatial and temporal evolution of a long term slow slip event: the 2006 Guerrero Slow Slip Event, *Geophys. J. Int.*, **184**(2), 816–828.
- Radiguet, M., Cotton, F., Vergnolle, M., Campillo, M., Walpersdorf, A., Cotte, N. & Kostoglodov, V., 2012. Slow slip events and strain accumulation in the Guerrero gap, Mexico, *J. Geophys. Res.*, **117**, B04305, doi:10.1029/2011JB008801.
- Rivet, D. *et al.*, 2014. Seismic velocity changes, strain rate and non-volcanic tremors during the 2009–2010 slow slip event in Guerrero, Mexico, *Geophys. J. Int.*, **196**, 447–460.
- Rogers, G. & Dragert, H., 2003. Episodic tremor and slip on the Cascadia subduction zone: The chatter of silent slip, *Science*, **300**, 1942–1943.
- Ross, Z. & Ben-Zion, Y., 2014. Automatic picking of direct P, S seismic phases and fault zone head waves, *Geophys. J. Int.*, **199**, 368–381.
- Rubin, A.M., 2011. Designer friction laws for bimodal slow slip propagation speeds, *Geochem. Geophys. Geosyst.*, **12**, Q04007, doi:10.1029/2010GC003386.
- Rubinstein, J.L. & La, M., Rocca, Vidale, J.E., Creager, K.C. & Wech, A.G., 2008. Tidal modulation of non-volcanic tremor, *Science*, **319**, 186–189.
- Rubinstein, J.L., Shelly, D.R. & Ellsworth, W.L., 2010. Non-volcanic tremor: A window into the roots of fault zones, in *New Frontiers in Integrated Solid Earth Sciences*, pp. 287–314, Springer.
- Segall, P., Rubin, A.M., Bradley, A.M. & Rice, J.R., 2010. Dilatant strengthening as a mechanism for slow slip events, *J. geophys. Res.*, **115**, B12305, doi:10.1029/2010JB007449.
- Shelly, D.R., Beroza, G.C. & Ide, S., 2007. Complex evolution of transient slip derived from precise tremor locations in western Shikoku, Japan, *Geochem. Geophys. Geosyst.*, **8**, Q10014, doi:10.1029/2007gc001640.
- Singh, S., Astiz, L. & Havskov, J., 1981. Seismic gaps and recurrence periods of large earthquakes along the Mexican subduction zone: a reexamination, *Bull. seism. Soc. Am.*, **71**(3), 827–843.
- Stockwell, R.G., Mansinha, L. & Lowe, R.P., 1996. Localization of the complex spectrum: the S transform, *IEEE Trans. Signal Process.*, **44**(4), 998–1001.
- Thomas, A.M., Nadeau, R.M. & Burgmann, R., 2009. Tremor-tide correlations and near-lithostatic pore pressure on the deep San Andreas fault, *Nature*, **462**(7276), 1048–1051.
- Vergnolle, M., Walpersdorf, A., Kostoglodov, V., Tregoning, P., Santiago, J.A., Cotte, N. & Franco, S.I., 2010. Slow slip events in Mexico revised from the processing of 11 year GPS observations, *J. geophys. Res.-Solid Earth*, **115**, B08403, doi:10.1029/2009jb006852.
- Voisin, C., Grasso, J.R., Larose, E. & Renard, F., 2008. Evolution of seismic signals and slip patterns along subduction zones: Insights from a friction lab scale experiment, *Geophys. Res. Lett.*, **35**, L08302, doi:10.1029/2008GL033356.
- Walpersdorf, A., Cotte, N., Kostoglodov, V., Vergnolle, M., Radiguet, M., Santiago, J.A. & Campillo, M., 2011. Two successive slow slip events evidenced in 2009–2010 by a dense GPS network in Guerrero, Mexico, *Geophys. Res. Lett.*, **38**, L15307, doi:10.1029/2011gl048124.
- Wech, A.G., Creager, K.C. & Melbourne, T.I., 2009. Seismic and geodetic constraints on Cascadia slow slip, *J. Geophys. Res.*, **114**, B10316, doi:10.1029/2008JB006090.
- Yamashita, T., 2013. Generation of slow slip coupled with tremor due to fluid flow along a fault, *Geophys. J. Int.*, **193**(1), 375–393.
- Zigone, D. *et al.*, 2012. Triggering of tremors and slow slip event in Guerrero, Mexico, by the 2010 Mw 8.8 Maule, Chile, earthquake, *J. geophys. Res.*, **117**, B09304, doi:10.1029/2012JB009160.
- Zigone, D., Voisin, C., Larose, E., Renard, F. & Campillo, M., 2011. Slip acceleration generates seismic tremor like signals in friction experiments, *Geophys. Res. Lett.*, **38**, L01315, doi:10.1029/2010GL045603.

## SUPPORTING INFORMATION

Additional Supporting Information may be found in the online version of this paper:

**Figure S1.** Response of the computational grid to the imposed large earthquakes (time marked by indicated by red arrows and line) in regions II and IV of Fig. 1(b). (a, b) Temporal evolution of seismicity in the seismological (a) and critical (b) fault sections. (c) Temporal evolution of the creep slip in the SSE patch.

**Figure S2.** (a, b) Creep slip evolution on the SSE patch for (a)  $23 \text{ yr} < t < 25 \text{ yr}$  and (b)  $60 \text{ yr} < t < 62 \text{ yr}$ . (c) North-south GPS data between 2009 and 2011 recorded at stations IGUA (blue) and MEZC (red). The station locations are indicated in Fig. 1(a). The simulated results have multiple small cycles with periods of a year or less which include smooth (a) and abrupt (b) changes. The detrended GPS time series has similar variations (c) with an overall smoother appearance due to the lower resolution

of the measurements at the surface. (<http://gji.oxfordjournals.org/lookup/suppl/doi:10.1093/gji/ggv174/-/DC1>)

Please note: Oxford University Press is not responsible for the content or functionality of any supporting materials supplied by the authors. Any queries (other than missing material) should be directed to the corresponding author for the paper.